AIMS Mathematics, 10(12): 28606–28628.
DOI: 10.3934/math.20251259
Received: 01 September 2025
Revised: 25 November 2025
Accepted: 27 November 2025
Published: 04 December 2025

https://www.aimspress.com/journal/Math

Research article

Computational insights and artificial neural network modeling of radiative boundary layer flows in tangent hyperbolic nanofluid

Khalid Masood*

Department of Mathematics and Statistics, College of Science, Imam Mohammad Ibn Saud Islamic University (IMISU), Riyadh 11623, Saudi Arabia

* **Correspondence:** Email: kmaali@imamu.edu.sa.

Abstract: This research examines the boundary-layer flow of a tangent hyperbolic nanofluid over a moving wedge, considering both viscous and radiative effects, in order to evaluate nanoparticle-enhanced thermal properties and non-Newtonian dynamics. The study combines nanofluid heat enhancement with non-Newtonian flow behavior, radiative thermal processes, and motile organism patterns to create an integrated mathematical framework that addresses current research gaps while proposing applications ranging from cooling systems to automotive thermal management, biomedical technology, and energy system design. The differential equations are transformed using similarity transformations before being solved numerically using MATLAB's fourth-order Runge-Kutta technique. The study uses artificial neural networks for prediction validation and findings via contour plots, three-dimensional graphs, and simplified visuals. The study shows that Weissenberg numbers increase fluid elasticity while decreasing drag, heat radiation effects expand temperature profiles while increasing thermal boundary thickness and shifts in thermophoresis, and Lewis numbers have a significant impact on chemical distributions by improving industrial studies of fluid dynamics.

Keywords: artificial neural network validation; boundary layer flow; tangent hyperbolic nanofluid; Runge–Kutta method
Mathematics Subject Classification: 76A02, 76A05, 76A20, 76W05

1. Introduction

Nanoparticle-containing base fluids represent a leading topic in fluid dynamics that focuses on

creating composite materials exhibiting enhanced thermal properties. When nanoparticles of metallic or oxide composition are incorporated into fluids, they dramatically affect both thermal and fluidic characteristics. The new applications take advantage of nanotechnology developments to boost material and heating properties, thus driving innovation among various industrial sectors. The heat transfer performance and skin friction behavior of traditional fluids improved substantially due to the work conducted by Omama et al. [1] on nanofluid flow through porous cylinders. The study by Imoro et al. [2] focused on pressure gradient effects on blood-based hybrid nanofluid flow behaviors in stenotic-aneurysmal arteries through fractional derivative analysis that demonstrated major changes in velocity, temperature and concentration fields. Wang et al. [3] indicate that an increase in the mixed convection parameter of nanofluid flow over a porous medium results in an increase in the temperature profile, while causing a decrease in the velocity profile. Mehboob et al. [4] investigated how Eyring-Powell nanofluids optimized bioconvective heat transfer in ciliated microchannels with higher viscosity led to decreased temperatures and stronger radiation parameters to increased temperatures. The laminar flow characteristics of cobalt ferrite containing Maxwell nanofluids were analyzed by Gupta et al. [5] under combined electromagnetohydrodynamic and thermal/solute stratification conditions.

The area of study of non-Newtonian fluids has rapidly grown in importance over the last twenty years. The velocity distributions corresponding to both slip and non-slip boundary conditions for non-Newtonian Maxwell fluids were established by Vieru and Zafar [6]. The tangent hyperbolic fluid model represents one of the core non-Newtonian fluid designs. Tangent hyperbolic nanofluids are characterized by a shear-thinning property, together with a high value of thermal conductivity, which makes them indispensable in maximizing cooling in heat exchangers, solar collectors, microchannels and rotating machines, as well as electronic apparatuses. In addition to this, they are also used in biomedical applications, especially in drug delivery to specific sites inside the body, and cooling of medical equipment, renewable energy systems, including photovoltaic/thermal collections and thermal energy storage systems, and in industrial processes, which include chemical reactor manipulation, lubrication, and coating processes. Their usefulness in automotive cooling systems, magnetohydrodynamic pumps, flows over porous media, and desalination, as well as waste-heat recovery, is enhanced by the improvement of their flow and heat-transfer properties, encouraging a wide range of industries to manage thermal and process efficiency, as illustrated in Figure 1. The field of chemical engineering benefits from using the tangent hyperbolic fluid model instead of traditional Newtonian model systems. The research by Ohaegbue et al. [7] established fundamental knowledge about complex thermal phenomena in combustible two-step tangent hyperbolic fluid flows through a complete analysis of heat transfer and dissipation. Spectrally hyperbolic partial differential equations (HPDEs) using the Galerkin method and approximate solutions using double shifted Jacobi Polynomials were examined by Doha et al. [8]. The convergence and error analyses of the hyperbolic equation employing HPDE were discussed in detail by Youssri et al. [9]. Sayed et al. [10] demonstrated that the third kind modified shifted Chebyshev polynomials' numerical solutions of hyperbolic equations align closely with exact solutions. Alqahtani et al. [11] and Ramasekhar et al. [12] investigated tangent hyperbolic nanofluids (THNFs) that exhibited excellent conductivity and stability properties that make THNFs suitable for electronic device cooling applications.

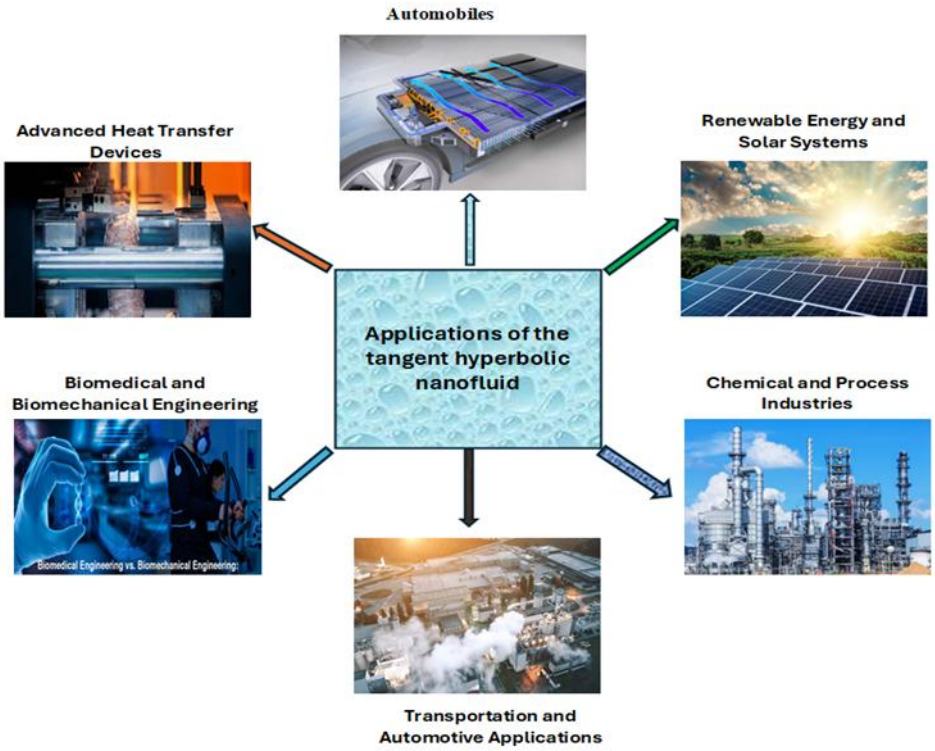

Figure 1. The utilization of tangent hyperbolic nanofluid across numerous disciplines.

Thermal radiation (TR) is the process by which energy is transferred via electromagnetic radiation released by objects that are characterized by temperatures higher than absolute zero. The phenomenon plays a key role in many crucial elements of daily life as well as industrial processes. As an example, thermal radiation can greatly influence heat transfer, which can be observed in technical systems, e.g., gas turbines, nuclear power plants, and other propulsion technologies provided by missiles and aircraft [13]. Radiation emits pulses as heat energy through spatial mediums as well as external nanoparticles. The rate of thermal dispersion, along with all other thermo-physical properties of a fluid, stems from its radiation characteristics. Alqahtani et al. [14] simulated heat transfer aspects in a magnetized porous medium under reduced gravity by analyzing thermal slip effects and radiative heat transfer together with viscous dissipation. Khan et al. [15] studied hybrid nanofluid behavior in magnetohydrodynamic (MHD) flow over porous stretching sheets leading to substantial heat transfer efficiency improvements. Zaman et al. [16] examined Williamson nanofluid flow through slender cylinders to show how diverse dimensionless parameters effect the evolution of velocity, temperature and concentration distributions. The flow characteristics of viscoelastic Maxwell fluids over porous plates revealed that increasing radiation and porous parameters enhance temperature profiles according to Sudarmozhi et al. [17]. Asogwa et al. [18] explained that the activation energy suppresses tangential hyperbolic concentration spreading of the nanofluid and that the rise in temperature in the hyperbolic tangential flow of nanofluid results from the growth of the Dufour effect. Anwar et al. [19] demonstrated how non-Newtonian Casson fluids behave during stagnation-point MHD convection by studying their complex magnetic field and fluid property and heat transfer interactions.

The primary objective of introducing self-moving microorganisms like gyrotactic, oxytactic and chemotactic microorganisms have a natural tendency to gather in the upper layer of the fluid medium due to their inherent motility. A dense surface layer becomes viable through this behavior and it might

trigger potential destabilization. These microorganisms undergo disintegration due to their upward swimming motion combined with the formation of macroscopic convection currents. Bioconvection presents significant importance to multiple operational sectors in manufacturing and biological sciences. The design of biological polymers and environmentally sustainable applications along with microbial-enhanced oil recovery systems requires extensive research experimentation and analytical enhancements to improve sustainable fuel cell technologies, biosensors, biotechnology and pharmaceutical systems, and ongoing mathematical programming. The research conducted by Rehman et al. [20] demonstrated that bioconvection in Casson nanofluid flow improved simultaneously as ferrous ferric oxide nanofluid was incorporated into the system. Mishra et al. [22] researched Jeffery fluid motion in ciliated vertical channels, while Agarwal et al. [22] studied Powell-Eyring fluid characteristics when exposed to exponentially stretching sheets. Sankari et al. [23] carried out a study investigating Williamson nanofluids under the same conditions as previous researchers, while Zhang et al. [24] analyzed water thermal enhancement in a porous medium via a suspension of hybrid nanoparticles. An investigation was conducted to integrate physical parameters which included MHD mixed convective Falkner's-Skan flow case study. Kumar et al. [25] developed a computational system to simulate the density distribution of Casson fluid-mobile microorganism mixes under thermal radiation conditions. The research by Gasmi et al. [26] evaluated the thermal behavior of mobile microorganisms in two-phase nanofluid flow using non-Newtonian fluid models that worked for both motionless and moving surfaces.

Artificial neural networks (ANNs) are machine learning techniques that are widely used to enhance thermal performance evaluations. The ability of ANNs to process historical data results in estimated outcomes that remain steady within a known, accurate area, matching human cognitive understanding. Kamsuwan et al. [27] have postulated an amalgamated computational fluid dynamics (CFD) simulation, when applied with artificial neural networks (ANNs), to investigate the operational efficacy of microchannel heat exchangers with the use of nanofluids. Qu et al. [28] applied an artificial neural network to replicate the thermal properties of hybrid nanofluids. Zahoor Raja et al. [29] also researched the advanced numerical computations made possible by artificial neural networks (ANNs) refined by a process known as the Levenberg-Marquardt algorithm (NN-BLMT) to study the theoretical implications of the quantity of heat generated in second-grade fluids caused by the Riga plate. Karmakar et al. [30] examined predictive behaviors by implementing an ionized fluid passing through an oscillating Riga plate with the help of ANNs. Lone et al. [31] assessed the aspects of irreversibility and the stagnation point flow of a hybrid nanofluid flow using a Riga plate with an artificial neural network (ANN). Rawat et al. [32] directed artificial neural networks to ternary hybrid nanofluid heat transfer analysis through particle swarm optimization.

1.1. State-of-the-art literature

Existing investigations into nanofluids and non-Newtonian fluids provide only a disjointed representation of reality. Previous research, primarily regarding nanoparticle enhanced thermal transfer, skin friction, radiation phenomena and geometries relating to porous or biomedical problems [1–5,13–19], as well as investigation of tangent hyperbolic formulations and related non-Newtonian approaches or spectral computational techniques [6–12], investigation of bioconvection in connection with motile microorganisms [20–26], research employing artificial intelligence for predicting of thermal flows [27–32], has been independently executed, and as a result, a unified and

coherent framework that simultaneously integrates tangent hyperbolic rheology, nanoparticles, thermal radiation, Brownian coefficient. The present research attempts to correct this ignored gap, by elaborating and solving such an integrated model and further simulating its thermo-bioconvective behavior using artificial neural network surrogates.

The current study integrates the enhanced thermal behavior of nanoparticle-enhanced tangent hyperbolic nanofluids with a mathematical-computational-artificial intelligence framework that examines radiative effects, Brownian motion, thermophoresis, and bioconvective characteristics, thereby addressing a critical knowledge gap in existing literature. Previous research studied nanofluids and non-Newtonian fluids separately, and a combined analysis of these phenomena under real-life flow systems remains unexplored. This research offers new insights about elastic, thermal, and mass transfer connections by applying a fourth-order Runge–Kutta numerical approach alongside similarity transformations with ANNs and three-dimensional graphics, enabling an accurate characterization of nonlinear thermo-fluidic interactions with a minimal increase in computational cost. The findings contribute to understanding complex fluid dynamics and provide valuable implications for technological applications, including electronic cooling devices, automotive heat control systems and biomedical devices, and energy harvesting systems, which form the foundation for experimental and industrial innovation.

2. Mathematical model

The research examines a two-dimensional boundary-layer flow of an incompressible laminar tangent hyperbolic nanofluid over a moving sharp wedge under viscous and radiative conditions. The $U(x) = U_\infty (x/L)^m$ expression defines the velocity distribution in the flow system over $m \le 1$, with L representing the characteristic length and m representing the wedge angle parameter that relates to the included angle $\pi\beta_1$ according to $m = \beta_1/(2-\beta_1)$. Here, β_1 acts as an indicator for pressure gradient changes.

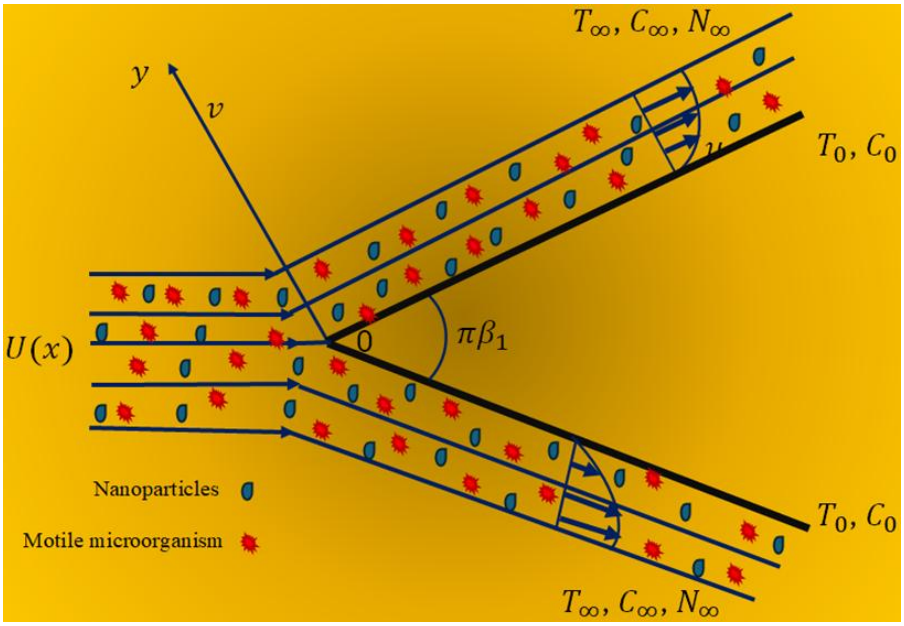

Figure 2. Model geometry.

A positive value of β_1 points to a negative pressure gradient (favorable), while a negative β_1 points to a positive pressure gradient (adverse). The solution shows singular characteristics at $x = 0$ only when $m < 0$, but it stays valid for all values of x in the case of m > 0. A convective heat transfer process maintains the wedge surface temperature constant, and the wedge bottom experiences heat transfer by convective fluid exchange at a temperature T_f with coefficient h. The wedge extends its surfaces at a uniform rate according to $U(x) = ax^m$ under laminar boundary layer conditions [30]. The positive $U(x)$ indicates service parallel alignment of the extending wave, while a negative value represents the opposing orientation for shrinking applications. The physical arrangement of the problem is depicted in Figure 2. All assumptions employed lead to a combination of continuity, and momentum, energy, and motile equations as follows [33]:

$$\frac{\partial u}{\partial x}+\frac{\partial v}{\partial y}=0, \tag{1}$$

$$u\frac{\partial u}{\partial x}+v\frac{\partial u}{\partial y}=-\frac{1}{\rho}\frac{dp}{dx}+\nu(1-n)\frac{\partial^2 u}{\partial y^2}+\sqrt{2}n\Gamma\nu\frac{\partial u}{\partial y}\frac{\partial^2 u}{\partial y^2}, \tag{2}$$

$$u\frac{\partial T}{\partial x}+v\frac{\partial T}{\partial y}=\alpha\frac{\partial^2 T}{\partial y^2}+\frac{\mu}{\rho C_p}\left(\frac{\partial u}{\partial y}\right)^2+\tau_1\left(D_B\frac{\partial C}{\partial y}\frac{\partial T}{\partial y}+\frac{D_T}{T_\infty}\left(\frac{\partial T}{\partial y}\right)^2\right)-\frac{1}{\rho C_p}\frac{\partial q_r^{**}}{\partial y}, \tag{3}$$

$$u\frac{\partial C}{\partial x}+v\frac{\partial C}{\partial y}=D_B\frac{\partial^2 C}{\partial y^2}+\frac{D_T}{T_\infty}\frac{\partial^2 T}{\partial y^2}, \tag{4}$$

$$u\frac{\partial N}{\partial x}+v\frac{\partial N}{\partial y}=D_m\frac{\partial^2 N}{\partial y^2}-\frac{bW_C}{(C_f-C_\infty)}\frac{\partial}{\partial y}\left(N\frac{\partial C}{\partial y}\right). \tag{5}$$

Similarity conditions applied in wedge geometry structures allow scientists to study physical system behaviors through investigations that require fewer time-consuming procedures. Model creation relies on these conditions to develop replicas of real-world situations while using simplified or scaled-down representations. The model must maintain behavioral consistency with the original system that predictions about reality become possible. Engineering and scientific experts can predict the reaction of wedge-shaped objects, like aircraft wings or dams, under specific conditions, such as fluid dynamics or pressure, through testing smaller or simplified prototypes due to similarity conditions. Such a research strategy reduces time expenses and saves resources and work effort while maintaining accuracy. Aerodynamic research allows scientists to utilize wind tunnel testing of small wedge-shaped wings, which predict actual wing performance during flight. The models and actual wings face proportionally corresponding forces and flow patterns through these established conditions.

Through the Roseland approximation, the radiative heat flux $\frac{\partial q_r^{**}}{\partial y}=-\frac{16\sigma_1 T_\infty^3}{3k^*}\frac{\partial^2 T^4}{\partial y^2}$ can be determined by considering k^* as the mean absorption coefficient and σ_1 as the Stefan-Boltzmann constant. Employing Taylor's sequence, we develop T^4 regarding the free stream temperature T while ignoring higher-order variables. One approximate value that may be attained from this is $T^4 = 4T_\infty^3 - 3T_\infty$, we find:

$$u\frac{\partial T}{\partial x}+v\frac{\partial T}{\partial y}=\frac{k}{\rho C_p}\frac{\partial^2 T}{\partial y^2}-\frac{\mu}{\rho C_p}\left(-\frac{\partial u}{\partial y}\right)^2-\tau_1\left(-D_B\frac{\partial c}{\partial y}\frac{\partial T}{\partial y}-\frac{D_T}{T_\infty}\frac{\partial^2 T}{\partial y^2}\right)+\frac{16\sigma_1 T_\infty^3}{3\rho C_p k^*}\frac{\partial^2 T}{\partial y^2}. \tag{6}$$

For the governing PDE, the boundary conditions are

$$\text{at}\quad y=0 \qquad \begin{aligned} &u=U(x)\frac{df}{dy}=cx^m, \quad v=v_w(x)=v_0(x^{-(1-m)})^{\frac{1}{2}}, \quad \frac{\partial T}{\partial y}=-(-T_\infty+T_f)\frac{h}{k},\\ &C=C_f,\ N=N_f. \end{aligned} \tag{7}$$

$$\text{at}\quad y\to\infty \quad u\to U(x), \quad \mathrm{T}\to T_\infty, \quad \mathrm{C}\to C_\infty, \quad N\to N_\infty. \tag{8}$$

Dimensionless ODEs result from transforming the PDEs with similarity transformations

$$\begin{aligned} &\eta=\sqrt{\frac{(m+1)U(x)}{2\nu x}}y, \ u=U(x)f'(\eta), \quad v=-\sqrt{\frac{(m+1)\nu U(x)}{2x}}\left(f(\eta)+\eta\frac{m-1}{m+1}f'(\eta)\right),\\ &\varphi(\eta)=\frac{(C-C_\infty)}{(C_f-C_\infty)}, \quad \theta(\eta)=\frac{(T-T_\infty)}{(T_f-T_\infty)}, \quad \chi(\eta)=\frac{(N-N_\infty)}{(N_w-N_\infty)}. \end{aligned} \tag{9}$$

The highly suitable conditions lead to a specific form of Eq (1), while Eqs (2) and (4)–(6) take corresponding forms. The identities of (1) lead the other expressions (2), (4), and (5) to become equivalent

$$(1-n)f'''+ff''-\beta_1(1-f'^2)+nWef'''f''=0, \tag{10}$$

$$\frac{1}{\mathrm{Pr}}\left(1+\frac{4}{3}Rd\right)\theta''+f\theta'-Nb\left(-\theta'\varphi'-\frac{Nt}{Nb}\theta'^2\right)+\mathrm{Pr}\,Ec\left(f''\right)^2=0, \tag{11}$$

$$\varphi''+Sc_b f\varphi'+\frac{Nt}{Nb}\theta''=0, \tag{12}$$

$$\chi''+Lbf\chi'-Pe\left((\chi+\Omega)\varphi''+\chi'\varphi'\right)=0. \tag{13}$$

The transformed boundary conditions for this problem issue appears in this sequence:

$$\eta=0 \quad f(0)=s, \ f'(0)=\lambda, \quad \varphi(0)=1, \quad \theta'=-Bi(-\theta+1), \ \chi(0)=1. \tag{14}$$

$$\text{At}\quad \eta\to\infty \quad f'(\eta)\to 1, \ \theta(\eta)\to 0, \quad \varphi(\eta)\to 0, \quad \chi(\eta)\to 0. \tag{15}$$

Where $Rd=\frac{16\sigma_1 T_\infty^3}{3kk^*}$ Thermal radiation parameter, $We=\Gamma\sqrt{\frac{(m+1)U^3}{2\nu l_c}}$ Weissenberg number,

$Nb = \dfrac{\tau_1 D_B (C_w - C_\infty)}{\vartheta}$ Brownian motion parameter, $Nt = \dfrac{\tau_1 D_T (T_w - T_\infty)}{\nu T_\infty}$ Thermophoretic parameter, $\Pr = \dfrac{\nu}{\alpha}$ Prandtl number, $\beta_1 = \dfrac{2m}{1+m}$, $Ec = \dfrac{U^2(x)}{C_p (T_f - T_\infty)}$ Eckert's number, $Sc_b = \dfrac{\nu}{D_B}$ Schmidt number.

Significant real-world parameters correspond to surface drag, diffusion, and thermal transmission constants, which are defined as follows:

$$Cf_x = \frac{\mu\left(\dfrac{\partial u}{\partial y} + \dfrac{\Gamma}{\sqrt{2}}\left(\dfrac{\partial u}{\partial y}\right)^2\right)\Big|_{y=0}}{\rho U^2}, Nu_x = \frac{-x\left(k\left(\dfrac{\partial T}{\partial y}\right) - q_r\right)}{k(T_f - T_\infty)}, Sh_x = \frac{-xq_m}{D_B(C_\infty - C_f)}. \tag{16}$$

The specified similarity transformation allowed us to solve these quantities, which produced the following results

$$\begin{aligned} &\mathrm{Re}_x^{1/2} Cf_x = \sqrt{\frac{m+1}{2}}\left((1-n)f''(0) + n\frac{We}{2}f''(0)\right), \qquad \mathrm{Re}_x^{-1/2} Nu_x = \sqrt{\frac{m+1}{2}}(-1 - \frac{4}{3}Rd)\theta'(0), \\ &\mathrm{Re}_x^{-1/2} Sh_x = -\sqrt{\frac{m+1}{2}}\varphi'(0). \end{aligned} \tag{17}$$

3. Numerical scheme and results validation

This investigation solves the governing equations of a tangent hyperbolic nanofluid moving along a wedge through the implementation of the fourth-order Runge–Kutta method while incorporating essential physical parameters. The tool in the MATLAB platform executes numerical analysis. We convert the higher-order differential equations through the introduction of auxiliary variables into a system of first-order ordinary differential equations (ODEs) to simplify the process. Processing begins by specifying ODE boundary conditions and initial values. Then, the ode45 built-in tool executes numerical computations for this system, which will work based on the Runge-Kutta method from the study of Palencia et al. [34]. The process terminates when the desired precision goal from the calculated residuals meets the required accuracy level [35]. The MATLAB Ann tool enables improved execution, data computation, and visualization of numerical methods and their resulting output.

1) $f = y_1$,

2) $f' = y_2$,

3) $f'' = y_3$,

4) $(1-n)dy_3 + y_1 y_3 + \beta(y_2^2 - 1) + nWedy_3 y_3 = 0$,

5) $\theta = y_4$,

6) $\theta' = y_5,$

7) $\frac{1}{\Pr}\left(1+\frac{4}{3}\right)dy_5 + y_1 y_5 - Nb\left(-y_5 y_7 - \frac{Nt}{Nb}{y_5}^2\right) - \Pr Ec(-y_3)^2 = 0,$

8) $\varphi = y_6,$

9) $\varphi' = y_7,$

10) $dy_7 + Sc_b y_1 y_7 + \frac{Nt}{Nb} dy_5 = 0,$

11) $E_1 = y_8,$

12) $E_1' = y_9,$

13) $dy_9 + Lby_1 y_9 + Pe(-(y_8 + \Omega)dy_7 - y_7 y_9) = 0.$

14) Boundary conditions

15) $y_1 = s, \quad y_2 = \lambda, \quad y_6 = 1, \quad y_5 = -Bi(1 - y_4), \; y_9 = 1,$

16) $y_2(\infty) \to 1, \; y_4(\infty) \to 0, \quad y_6(\infty) \to 0, \; y_8(\infty) \to 0.$

The numerical error was determined by re-executing the Runge-Kutta [36,37] method with a modified absolute tolerance ($1x10^{-6}$) and a more strict tolerance ($1x10^{-10}$) on the domain $\eta \in [0, 10]$. The variations in the values of the shear coefficients observed were below the 0.4% threshold for each of the conditions, thus confirming the strength, convergence, and stability of the present study solution.

3.1. Artificial neural network

For outcomes using ANN-based methodologies, specifically on the Levenberg-Marquardt strategy, the dataset division that is provided by the Runge-Kutta fourth-order methodology was split into training, testing, and validation sets. In this analysis, 70% of the data set was used as training data and the remaining 30% was used as test and validation data. The training process was stopped when the network propagation exceeded a specified threshold that was checked using a validation process. This did not disrupt the training phase, thus allowing the assessment of the network performance to be carried out at regular intervals during and after the training process. Figure 3 illustrates the neural network structures of the current study. The results produced by the ANN were later checked with the help of the computation of the related errors. The divergence of the proposed methodology was fast, and stability and reliability were also good compared to traditional methods. The ANN was consistent, had no flaws, and was skilled in high-accuracy performance at an efficient rate. The ANN-based solution strategy was far superior to conventional methods in solutions, achieving the same order of magnitude faster predictions and approximations than traditional solvers, which, in many cases, required long periods to solve a system of ordinary differential equations. The

efficacy, reliability, and efficiency of the networks in the fluid flow analysis were evaluated using regression statistics, mean square errors of the training, testing, and validation set, error histograms of complex simulations, and accuracy assessment. A comparative analysis was performed using LM on basis of metrics like regression fitness, mean square error (MSE), and error histograms. Moreover, the application of the Levenberg-Marquardt algorithm was done in the MATLAB machine learning toolbox, where ANN was combined with the Runge-Kutta fourth-order process to investigate the behaviors of fluids and test the findings. R^2 values of 100% will represent a good fit between the response and predictors.

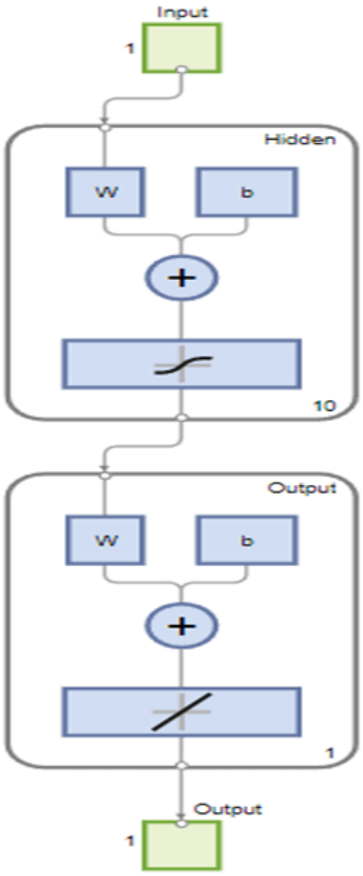

Figure 3. Neural network structure.

Table 1 details the results of the current study, revealing that the value for $-f''(0)$ for various values of β with the previous studies carried out by [37–39], thus proving the validity of the model. Table 2 shows that the Levenberg-Marquardt presents impressive accuracy regardless of the evaluated architectures, including 10 and 15 hidden neurons, which produce extremely low mean squared error (MSE) and perfect correlation (R = 1) for training, validation, and testing data. Moreover, increasing in the number of hidden neurons to 20 leads to a slight decrease in performance (MSE is higher and R is less than 1). Figure 4 demonstrates the legitimacy of the artificial neural network.

Table 1. Comparison of current and published studies of skin friction $-f''(0)$.

β	[38]	[39]	[40]	Present work
0.0	0.469600	0.4696	0.469600	0.46960
0.1	0.587080	0.5870	0.587035	0.58706
0.3	0.774724	0.7780	0.774757	0.77478
0.5	0.927905	0.9277	0.927681	0.92769
1.0	1.238589	1.2323	1.232588	1.23259

Table 2. Performance of Levenberg–Marquardt ANN for different numbers of hidden neurons (MSE and R).

Hidden neurons	Gradient	Performance	Mu	MSE		R
10	$9.9e^{-8}$	$3.56e^{-11}$	$9.9e^{-8}$	Train	$3.5569e^{-11}$	1
				Validation	$9.5004e^{-11}$	1
				Test	$3.6567e^{-11}$	1
15	$9.9e^{-8}$	$2.9561e^{-12}$	$1e^{-11}$	Train	$2.9561e^{-12}$	1
				Validation	$3.3500e^{-11}$	1
				Test	$3.7641e^{-11}$	1
20	$2.2e^{-5}$	$8.66e^{-07}$	$1e^{-8}$	Train	$2.7291e^{-06}$	0.9999
				Validation	$4.1625e^{-06}$	0.9999
				Test	$1.5798e^{-05}$	0.9996

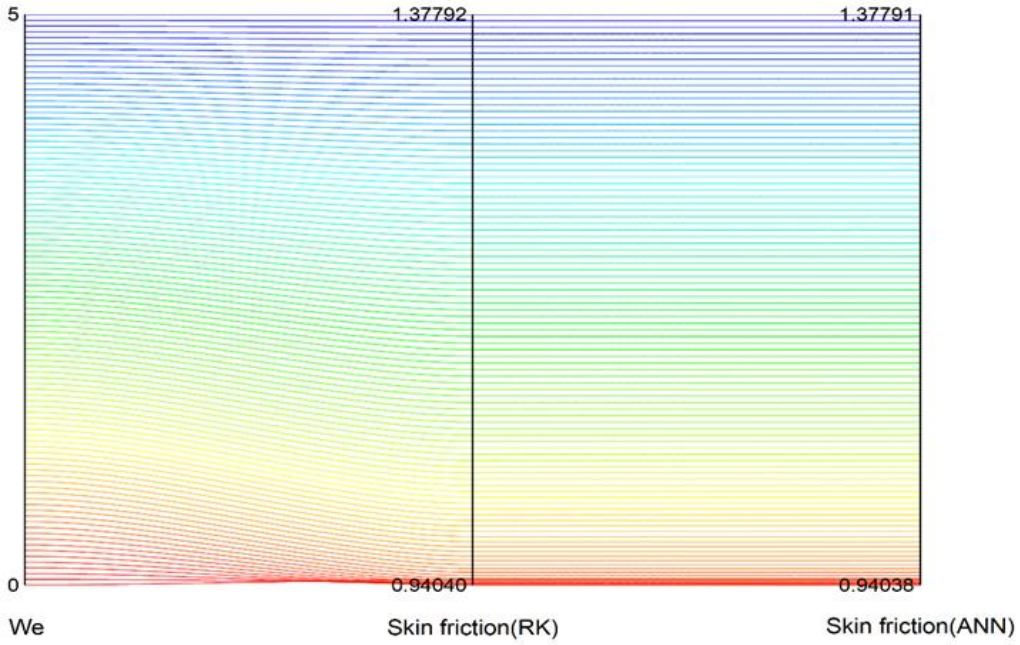

Figure 4. Comparison of ANN and simulation results.

Figure 5 demonstrates a combined computational and neural network model that analyzes radiative tangential hyperbolic tangent nanofluid flow over a moving wedge. The experimental data, together with the ANN's ability to project non-linear behavior, led to validated results, confirmed by contour plots, three-dimensional streamlines, and accurate Nusselt number and skin friction coefficient.

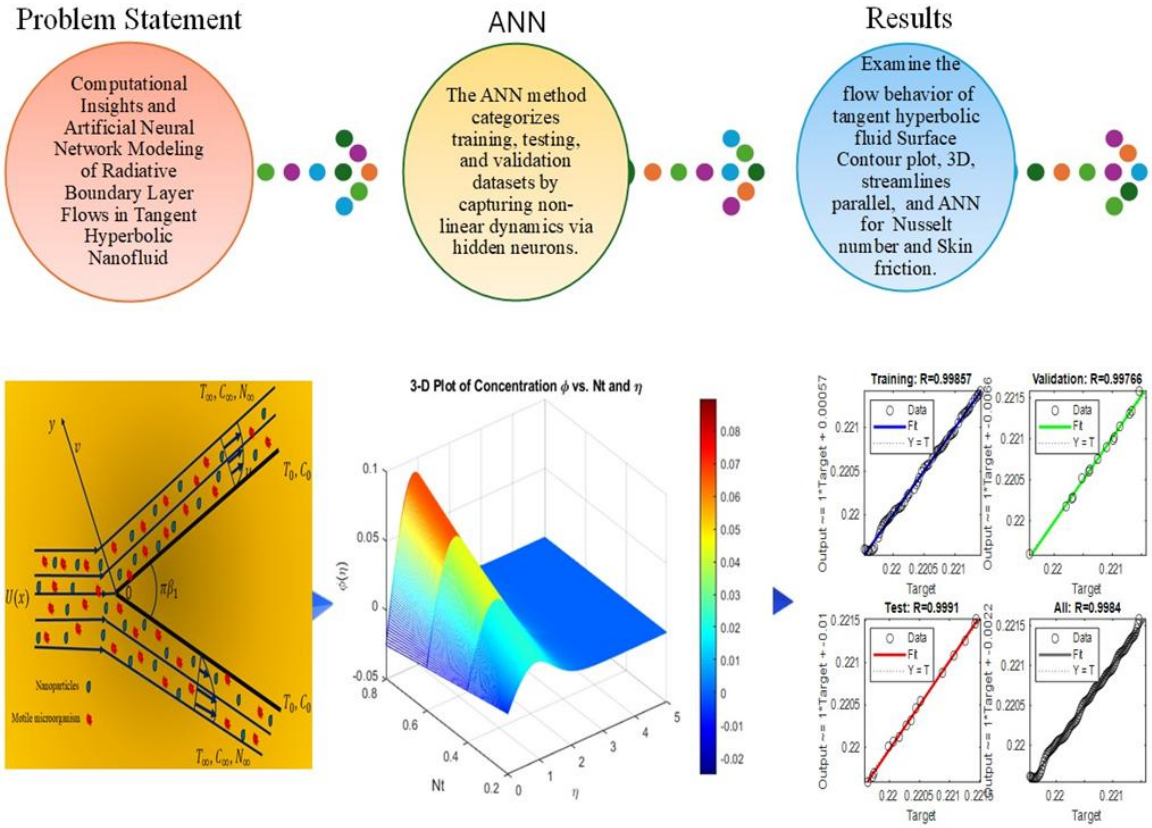

Figure 5. Flow chart.

4. Results and discussion

4.1. ANN and various factors influence on the flow profiles

The Weissenberg number (We) affects velocity, as shown in Figures 6(a), 6(b), and 8(a) through combination plots along with three-dimensional and two-dimensional representations. The Weissenberg number (We) is a ratio used to measure the ratio between fluid relaxation time and flow time. Therefore, a high We indicates that the microstructure of the tangent hyperbolic fluid (contained by polymer-like chains or aggregates) supports a longer deformation and produces larger elastic normal stresses. These stresses oppose the large local shear rates as well as smooth, sharp changes in deformation and consequently minimize the velocity gradient close to the walls and flatten the velocity profile. The temperature profiles under different radiation levels (Rd) are shown in Figures 6(c), 6(d), and 8(b), through both contour plots and three-dimensional and two-dimensional display formats. The intensification of the radiation parameter increases the strength of radiative heat flux, providing an extra energy transportation mechanism, increasing the temperature of the fluid. This additional radiative heating reduces the temperature gradient close to the wall and enhances a stronger diffusion of heat across the surface, therefore boosting the thickness of the thermal boundary layer and indicating

a greater radiative effect on the overall distribution of heat in the flow.

The concentration profile changes in response to the thermophoresis parameter (Nt) are presented through contour plots (Figure 7(a)) and three-dimensional (Figure 7(b)) and two-dimensional illustrations (Figure 8(c)). The thermophoresis parameter (Nt) increases the strength of the thermophoretic force that causes the movement of nanoparticles between high-temperature and low-temperature regions. This unidirectional migration will cause an increase in the concentration of particles near the cooler surface and, therefore, a reduction of local concentration gradients, thus increasing the concentration boundary layer, which will increase the concentration profile.

The Lewis number (Lb) effect on motile profiles is shown in Figures 7(c), 7(d), and 8(d) through contour plots and three-dimensional and two-dimensional visuals. When the Lewis number increases, the thermal diffusivity gains superiority over mass diffusivity in the system. Higher heat transport speed shortens the concentration gradients responsible for motile accumulation, thus reducing the presence of motile cells within the flow.

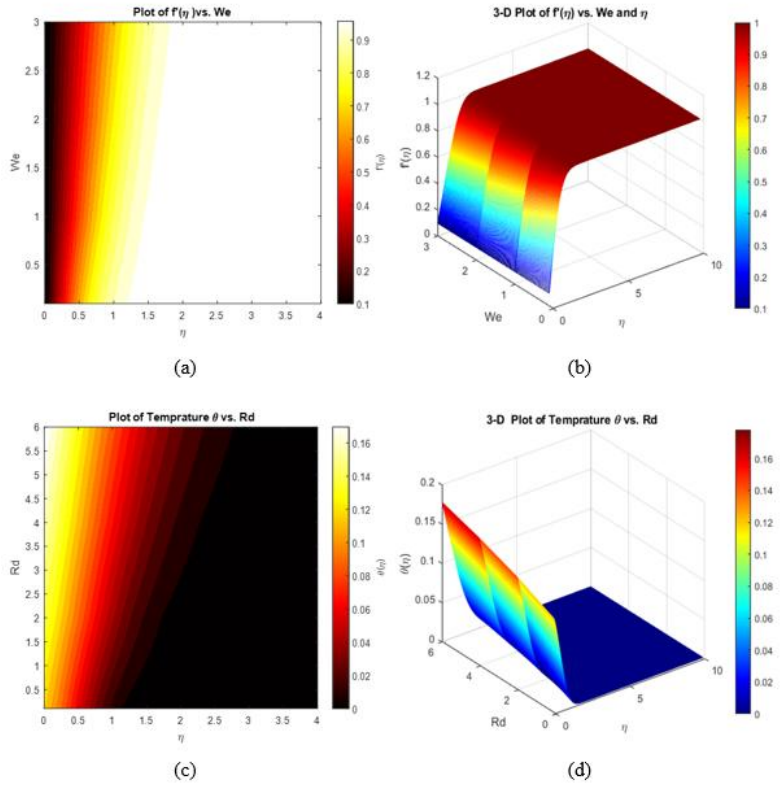

Figure 6. Impact of We and Rd on velocity and temperature profiles.

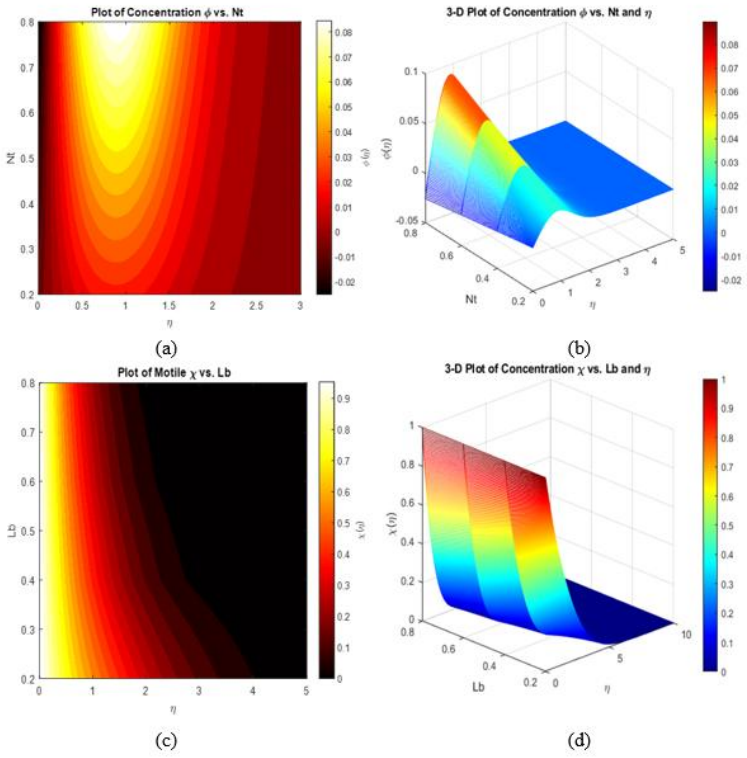

Figure 7. Impact of Nt and Lb on concentration and motile profiles.

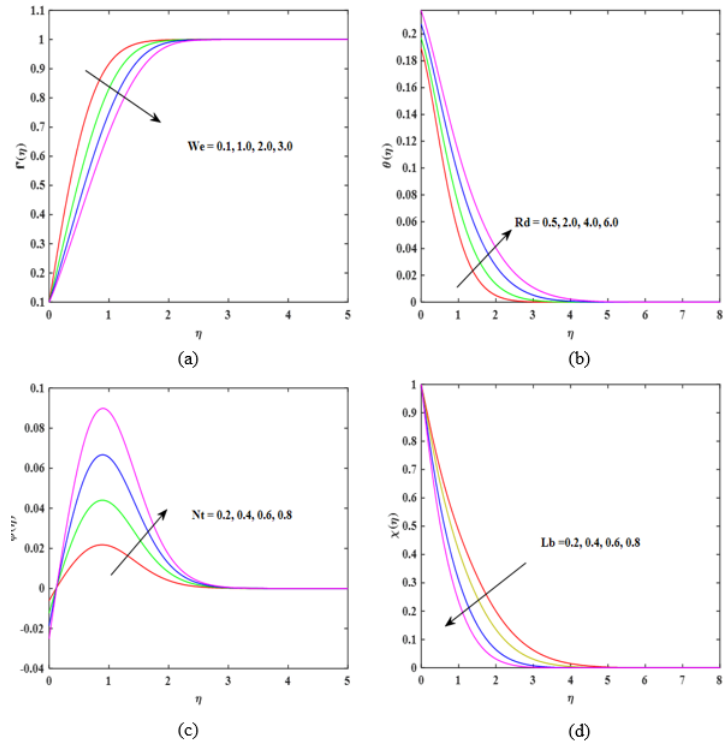

Figure 8. 2-D plot for We, Rd, Nt, and Lb on velocity, temperature, concentration, and motile profiles.

Low error values in Figure 9(a) indicate model consistency across different datasets; Figure 9(b) shows that the model reaches convergence through error reduction. The strong relationship between expected values and target results is clear in Figure 9(c). Figure 9(d) shows that the Weissenberg number displays a direct relationship with velocity profile reduction because it leads to diminished skin friction factors. The physical properties of increased Weissenberg number result in fluid elasticity that leads to smoothed velocity gradients adjacent to the wall, while simultaneously reducing wall shear stress and consequently lowering skin friction. Figures 8 and 9 also demonstrate the effect of We and n on skin friction. Figures 10(a) and 10(b) illustrate that skin friction values are enhanced as the values of We rise, but a reverse behavior is seen for n, as shown in Figures 11(a) and 11(b). Figure 12(a) demonstrates that most errors from training, validation, and testing datasets focus on lower value ranges, which indicate reliable prediction outcomes. The mean squared error shown in Figure 12(b) keeps declining through each epoch, demonstrating that the model was successfully trained. Figure 12(c) (regression) reveals an excellent predictive agreement between calculated and target values that signifies high modeling precision, and Figure 12(d) validates precise model data alignment. Physically, the increased parameter (Nt) causes particles to move more strongly from warm areas, thus lowering the wall temperature gradient and reducing the Nusselt number model data alignment. Figure 13 highlights the effects of the Brownian motion (Nb) and Nt parameters on Nusselt numbers. Figures 13(a) and 13(b) indicate that the value of the Nusselt number decreases as the values of Nb and Nt increase. An increase in the thermophoresis parameter (Nt) enhances the thermophoretic movement of the nanoparticles on the heated wall to the cooler core and consequently reinforces the transfer of energy out of the surface by the migrating particles. This redistribution of the thermal energy helps to smooth the temperature field near the wall, enhances the thickness of a thermal boundary layer, and decreases the temperature gradient at the wall; therefore, the value of the local Nusselt number decreases with Nt. Figure 14 demonstrates a comparison between streamline patterns for cases where $We = 0.1$ and $We = 0.2$. When the Weissenberg number becomes higher, the viscoelastic effects strengthen and produce alterations in flow structures through which streamline changes occur alongside boundary compression, leading to increased velocity gradients closest to walls. Figure 15 shows $n = 0.1$ and $n = 0.2$ streamline distributions. Shear-thinning properties of the fluid increase when the power-law index (n) decreases, which causes streamlined displacement and compression in high shear regions. The accentuated velocity gradient develops mostly in close proximity to the boundaries because of these changes.

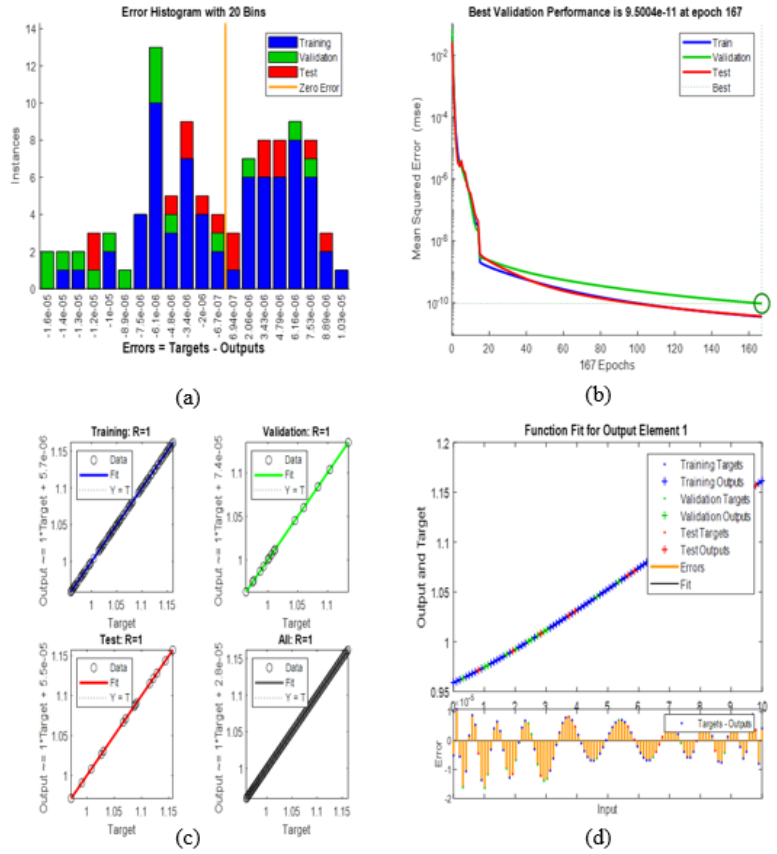

Figure 9. Ann's plot for *We* on skin friction.

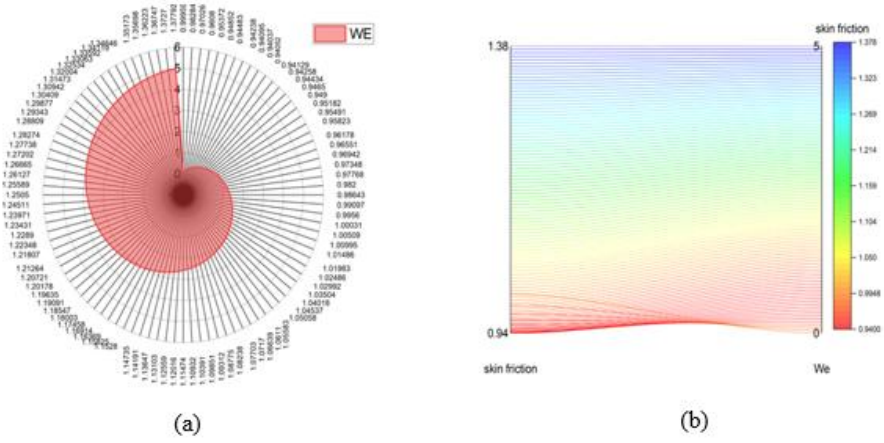

Figure 10. Effect of *We* on skin friction.

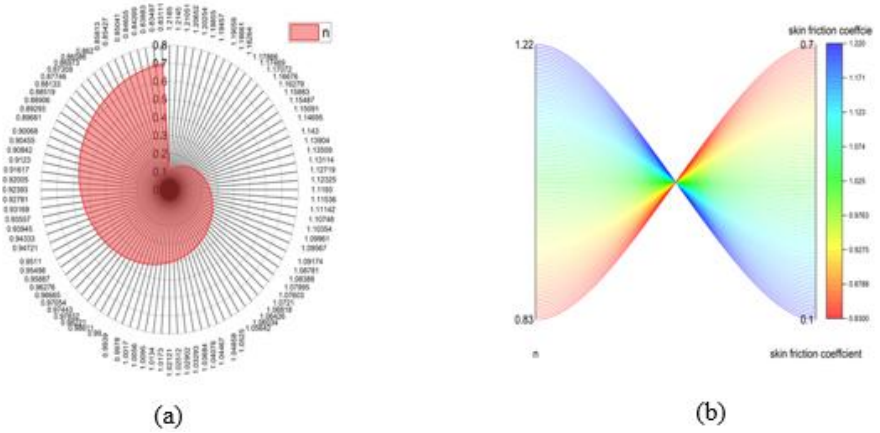

Figure 11. Effect of n on skin friction.

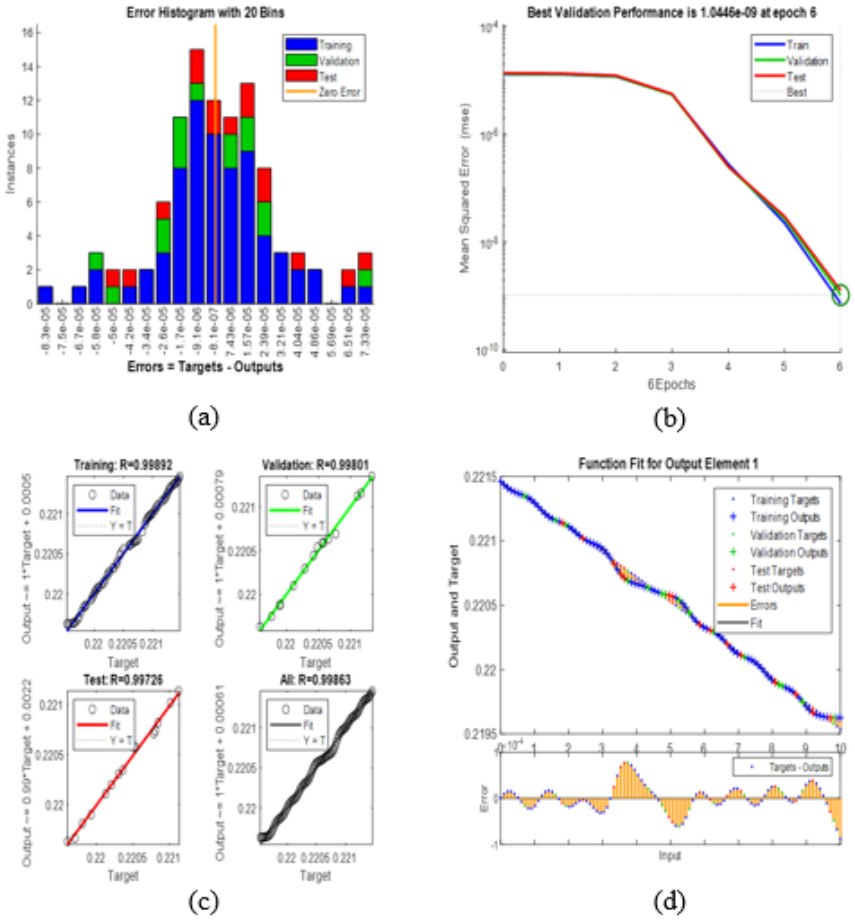

Figure 12. Ann's plot for Nt on Nusselt number.

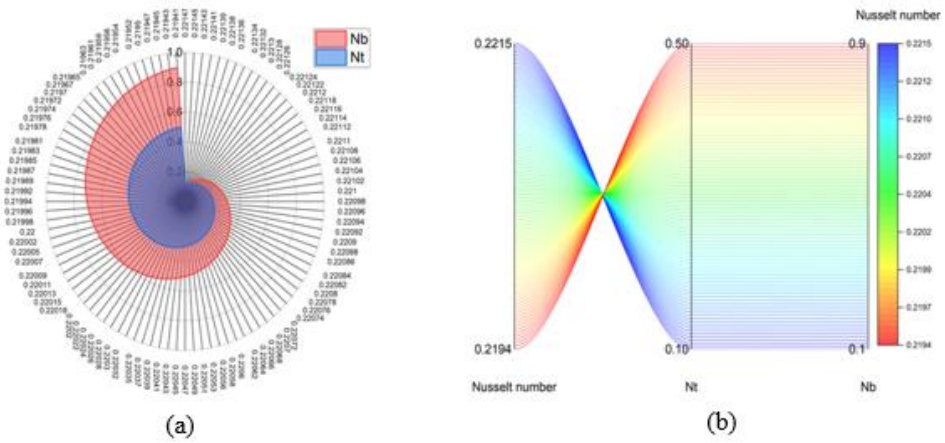

Figure 13. Effect of Nb & Nt on the Nusselt number.

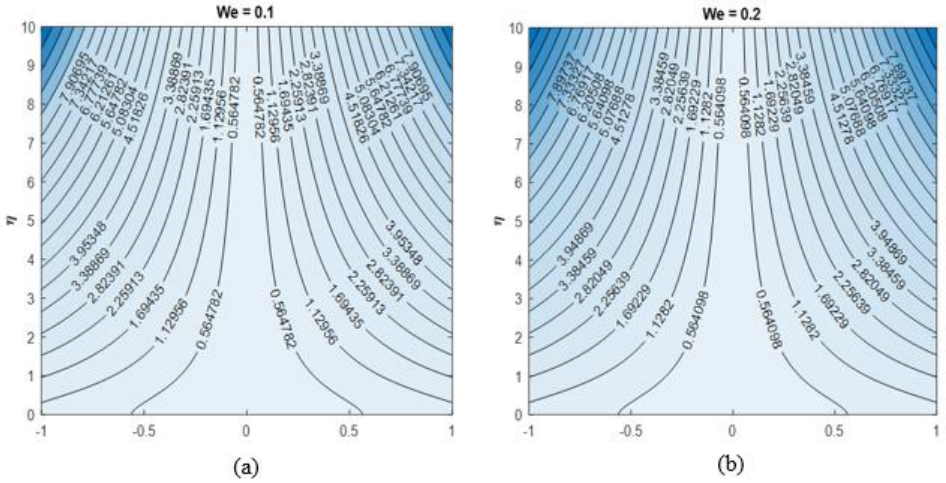

Figure 14. Streamlines for $we = 0.1$ and $we = 0.2$.

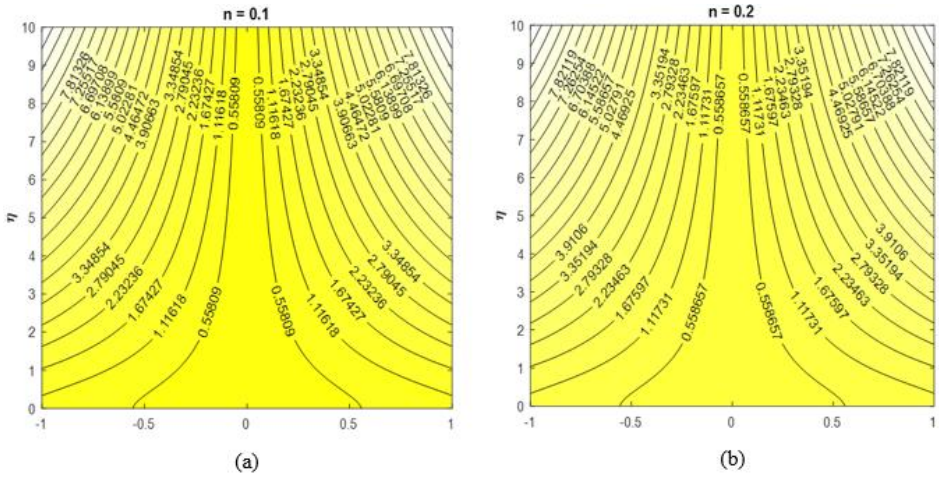

Figure 15. Streamlines for $n = 0.1$ and $n = 0.2$.

4.2. Grid independence test and comparison of results

In Table 3, fine and finer mesh results are compared values of the Nusselt number coincide in all cases of We. The grid independence test is met because no additional refinement results in any change; thus, the fine grid is sufficient to produce the correct simulation.

Table 3. Grid independence test.

We	Results for fine mesh	Results for finer mesh
	Nusselt number	Nusselt number
1	0.2210	0.2210
2	0.2261	0.2261
3	0.2290	0.2290
4	0.2310	0.2310

5. Conclusions

This study investigates the two-dimensional boundary-layer flow of a laminar tangent hyperbolic nanofluid over a moving wedge under viscous and radiative conditions. The combination of 3D graphs along with contour plots and streamline visualizations delivers a complete understanding about flow dynamics, as follows.

- We (Weissenberg number): An increase in the Weissenberg number makes the fluid more elastic, thus leading to reduced velocity gradients near the border and decreased skin friction.
- Rd (Radiation parameter): The increase of radiation parameter strengthens the heat transfer process through the production of expanded temperature zones and thickened thermal boundary layers that result in a higher Nusselt number.
- Nt (Thermophoresis parameter): The enhanced thermophoresis parameter strengthens thermophoretic forces between nanoparticles as they move towards cooler areas and increase the concentration boundary layer.
- Lb (Lewis number): Higher Lewis number values indicate that thermal diffusivity dominates over mass diffusivity, causing concentration gradients and motile-cell accumulation to become less pronounced.
- Skin friction: As the Weissenberg number increases, the skin friction factor increases, indicating higher wall shear stress under the studied conditions.
- Nusselt number (for Nt): Increased Nt parameter results in a diminished wall temperature difference that equals a Nusselt number reduction, which represents inefficient convective heat transfer operation.
- Streamlines: Visual streamline examinations demonstrate that non-Newtonian actions cause large boundary-region displacements and compression patterns.
- Artificial neural networks (ANNs): Integrating ANNs enhances predictive validation of performance parameters, thus reducing the need for exhaustive numerical investigations.
- Future scope: The study sets the groundwork for future investigations in non-Newtonian nanofluid dynamics, which will aid the optimization of cooling systems across multiple industrial sectors.
- A physically informed neural network is one of the limitations of the current study.

Nomenclature

Name	Units	Symbol	Name	Units	Symbol
Cartesian coordinate components	(m)	(x,y)	Velocity components	(m/s)	(u,v)
Thermal radiation parameter	-	R	Brownian motion parameter	-	Nb
Weissenberg number	-	We	Specific heat	$(J/Kg.K)$	C_p
Eckert's number	-	Ec	Thermal diffusivity	(m^2/s)	α
Radiation heat flux	$(W\ m^2)$	q_r	Schmidt number	-	Sc_b
Density	(kg/m^3)	ρ	Density ratio of the motile microorganisms	-	Ω
Peclet number	-	Pe	Brownian diffusion	-	D_B
Lewis number	-	Lb	Thermophoretic parameter	-	Nt

Use of Generative-AI tools declaration

The author declares that he have not used Artificial Intelligence (AI) tools in the creation of this article.

Acknowledgments

This work was supported and funded by the Deanship of Scientific Research at Imam Mohammad Ibn Saud Islamic University (IMSIU) (grant number IMSIU-DDRSP2503).

Conflict of interest

The author has no conflict of interest.

References

1. M. Omama, A. A. Arafa, A. Elsaid, W. K. Zahra, MHD tri-hybrid nanofluid blood flow in a porous cylinder: Insights from fractional relaxation modeling with thermal radiation and slip velocity boundary condition, *ZAMM-Z. Angew. Math. Me.*, **105** (2025), e202400375. https://doi.org/10.1002/zamm.202400375
2. I. Imoro, C. J. Etwire, R. Musah, Effect of pressure on MHD flow of blood-based hybrid nanofluid through an inclined Stenotic–Aneurysmal artery, *J. Appl. Math.*, **2025** (2025), 8847298. https://doi.org/10.1155/jama/8847298
3. F. Z. Wang, A. M. Saeed, V. Puneeth, N. A. Shah, S. M. Anwar, K. Geudri, et al., Heat and mass transfer of Ag-H2O nano-thin film flowing over a porous medium: A modified Buongiorno's model, *Chinese J. Phys.*, **84** (2023), 330–342. https://doi.org/10.1016/j.cjph.2023.01.001
4. J. Mehboob, R. Ellahi, S. M. Sait, N. S. Akbar, Optimizing bioconvective heat transfer with MHD Eyring–Powell nanofluids containing motile microorganisms with viscosity variability and porous media in ciliated microchannels, *Int. J. Numer. Method. H.*, **35** (2024), 825–846. https://doi.org/10.1108/HFF-11-2024-0838

5. S. Gupta, P. K. Jain, V. S. Sangtani, V. K. Singhal, EMHD flow of double stratified 3D-cobalt ferrite based Maxwell nanoliquid flow over an exponentially stretching surface, *Phys. Scr.*, **100** (2025), 035202. https://doi.org/10.1088/1402-4896/ada4f3
6. D. Vieru, A. A. Zafar, Some Couette flows of a Maxwell fluid with wall slip condition, *Appl. Math. Inform. Sci.*, **7** (2013), 209–219, https://doi.org/10.12785/amis/070126
7. A. D. Ohaegbue, S. O. Salawu, R. A. Oderinu, E. O. Fatunmbi, A. O. Akindele, Thermal dissipation of two-step combustible tangent hyperbolic fluid with quadratic Boussinesq approximation and convective cooling, *Results in Materials*, **22** (2024), 100565. https://doi.org/10.1016/j.rinma.2024.100565
8. E. H. Doha, R. M. Hafez, Y. H. Youssri, Shifted Jacobi spectral-Galerkin method for solving hyperbolic partial differential equations, *Comput. Math. Appl.*, **78** (2019), 889–904. https://doi.org/10.1016/j.camwa.2019.03.011
9. Y. H. Youssri, R. M. Hafez, Exponential Jacobi spectral method for hyperbolic partial differential equations, *Math. Sci.*, **13** (2019), 347–354. https://doi.org/10.1007/s40096-019-00304-w
10. S. M. Sayed, A. S. Mohamed, E. M. Abo-Eldahab, Y. H. Youssri, Spectral framework using modified shifted Chebyshev polynomials of the third-kind for numerical solutions of one-and two-dimensional hyperbolic telegraph equations, *Bound. Value Probl.*, **2025** (2025), 7. https://doi.org/10.1186/s13661-024-01987-4
11. A. M. Alqahtani, M. Bilal, M. B. Riaz, W. Chammam, J. Shafi, M. U. Rahman, et al., Forced convective tangent hyperbolic nanofluid flow subject to heat source/sink and Lorentz force over a permeable wedge: numerical exploration, *Nanotechnol. Rev.*, **13** (2024), 20240014. https://doi.org/10.1515/ntrev-2024-0014
12. G. Ramasekhar, M. Jawad, A. Divya, S. Jakeer, H. A. Ghazwani, M. R. Almutiri, et al., Heat transfer exploration for bioconvected tangent hyperbolic nanofluid flow with activation energy and joule heating induced by Riga plate, *Case Stud. Therm. Eng.*, **55** (2024), 104100. https://doi.org/10.1016/j.csite.2024.104100
13. J. Madhu, J. K. Madhukesh, I. Sarris, B. C. Prasannakumara, G. K. Ramesh, N. A. Shah, et al., Influence of quadratic thermal radiation and activation energy impacts over oblique stagnation point hybrid nanofluid flow across a cylinder, *Case Stud. Therm. Eng.*, **60** (2024), 104624. https://doi.org/10.1016/j.csite.2024.104624
14. B. Alqahtani, E. R. El-Zahar, M. B. Riaz, L. F. Seddek, A. Ilyas, Z. Ullah, et al., Computational analysis of microgravity and viscous dissipation impact on periodical heat transfer of MHD fluid along porous radiative surface with thermal slip effects, *Case Stud. Therm. Eng.*, **60** (2024), 104641. https://doi.org/10.1016/j.csite.2024.104641
15. Z. H. Khan, W. A. Khan, S. M. Ibrahim, K. Swain, Z. T. Huang, Impact of multiple slips and thermal radiation on heat and mass transfer in MHD Maxwell hybrid nanofluid flow over porous stretching sheet, *Case Stud. Therm. Eng.*, **61** (2024), 104906. https://doi.org/10.1016/j.csite.2024.104906
16. S. U. Zaman, M. N. Aslam, M. B. Riaz, A. Akgul, A. Hussan, Williamson MHD nanofluid flow with radiation effects through slender cylinder, *Results in Engineering*, **22** (2024), 101966. https://doi.org/10.1016/j.rineng.2024.101966
17. K. Sudarmozhi, D. Iranian, Q. M. Al-Mdallal, Revolutionizing energy flow: Unleashing the influence of MHD in the presence of free convective heat transfer with radiation, *International Journal of Thermofluids*, **22** (2024), 100662. https://doi.org/10.1016/j.ijft.2024.100662

18. K. K. Asogwa, B. S. Goud, N. A. Shah, S. J. Yook, Rheology of electromagnetohydrodynamic tangent hyperbolic nanofluid over a stretching riga surface featuring dufour effect and activation energy, *Sci. Rep.*, **12** (2022), 14602. https://doi.org/10.1038/s41598-022-18998-9
19. M. S. Anwar, M. S. Alqarni, M. Irfan, Exploring the marvels of heat transfer: MHD convection at a stagnation point in non-Newtonian fluid with yield stress and chemical reactions, *Chinese J. Phys.*, **89** (2024), 1299–1308. https://doi.org/10.1016/j.cjph.2024.01.030
20. K. U. Rehman, N. Fatima, W. Shatanawi, N. Kousar, Mathematical solutions for coupled nonlinear equations based on bioconvection in MHD Casson nanofluid flow, *AIMS Mathematics*, **10** (2025), 598–633. https://doi.org/10.3934/math.2025027
21. N. K. Mishra, P. Sharma, B. K. Sharma, B. Almohsen, L. M. Pérez, Electroosmotic MHD ternary hybrid Jeffery nanofluid flow through a ciliated vertical channel with gyrotactic microorganisms: Entropy generation optimization, *Heliyon*, **10** (2024), e25102. https://doi.org/10.1016/j.heliyon.2024.e25102
22. P. Agarwal, R. Jain, K. Loganathan, Thermally radiative flow of MHD Powell-Eyring nanofluid over an exponential stretching sheet with swimming microorganisms and viscous dissipation: A numerical computation, *International Journal of Thermofluids*, **23** (2024), 100773. https://doi.org/10.1016/j.ijft.2024.100773
23. M. S. Sankari, M. E. Rao, Z. E. Shams, S. Algarni, M. N. Sharif, T. Alqahtani, et al., Williamson MHD nanofluid flow via a porous exponentially stretching sheet with bioconvective fluxes, *Case Stud. Therm. Eng.*, **59** (2024), 104453. https://doi.org/10.1016/j.csite.2024.104453
24. K. Z. Zhang, N. A. Shah, M. Alshehri, S. Alkarni, A. Wakif, S. M. Eldin, Water thermal enhancement in a porous medium via a suspension of hybrid nanoparticles: MHD mixed convective Falkner's-Skan flow case study, *Case Stud. Therm. Eng.*, **47** (2013), 103062. https://doi.org/10.1016/j.csite.2023.103062
25. K. A. Kumar, A computational model for the density of motile micro-organisms in the casson fluid flow with thermal radition: A computational model for the density of motile micro-organisms in the casson fluid flow with thermal radition, *J. Nav. Archit. Mar. Eng.*, **21** (2024), 79–86. https://doi.org/10.3329/jname.v21i1.70396
26. H. Gasmi, A. M. Obalalu, A. O. Akindele, S. A. Salaudeen, U. Khan, A. Ishak, et al., Thermal performance of a motile-microorganism within the two-phase nanofluid flow for the distinct non-Newtonian models on static and moving surfaces, *Case Stud. Therm. Eng.*, **58** (2024), 104392. https://doi.org/10.1016/j.csite.2024.104392
27. C. Kamsuwan, X. L. Wang, L. P. Seng, C. K. Xian, R. Piemjaiswang, P. Piumsomboon, et al., Simulation of nanofluid micro-channel heat exchanger using computational fluid dynamics integrated with artificial neural network, *Energy Rep.*, **9** (2023), 239–247. https://doi.org/10.1016/j.egyr.2022.10.412
28. Y. R. Qu, D. J. Jasim, S. M. Sajadi, S. Salahshour, M. K. Khabaz, A. Rahmanian, et al., Artificial neural network modeling of thermal characteristics of WO_3-CuO (50:50)/water hybrid nanofluid with a back-propagation algorithm, *Mater. Today Commun.*, **38** (2024), 108169. https://doi.org/10.1016/j.mtcomm.2024.108169
29. M. A. Z. Raja, M. Shoaib, E. R. El-Zahar, S. Hussain, Y.-M. Li, M. I. Khan, et al., Heat transport in entropy-optimized flow of viscoelastic fluid due to Riga plate: analysis of artificial neural network, *Wave. Random Complex*, **35** (2022), 1077–1096. https://doi.org/10.1080/17455030.2022.2028933

30. P. Karmakar, S. Das, N. Mahato, A. Ali, R. N. Jana, Dynamics prediction using an artificial neural network for a weakly conductive ionized fluid streamed over a vibrating electromagnetic plate, *Eur. Phys. J. Plus*, **139** (2024), 407. https://doi.org/10.1140/epjp/s13360-024-05197-w
31. S. A. Lone, Ar. Khan, T. Gul, S. Mukhtar, W. Alghamdi, I. Ali, Entropy generation for stagnation point dissipative hybrid nanofluid flow on a Riga plate with the influence of nonlinear convection using neural network approach, *Colloid Polym. Sci.*, **302** (2024), 745–770. https://doi.org/10.1007/s00396-024-05227-0
32. S. K. Rawat, M. Yaseen, M. Pant, C. S. Ujarari, Designing artificial intelligence computing techniques to study heat transfer of a ternary hybrid nanofluid flow: Application of particle swarm optimization and artificial neural network, *Mod. Phys. Lett. B*, **39** (2025), 2550114. https://doi.org/10.1142/s0217984925501143
33. S. Venkateswarlu, B. H. Babu, M. V. Krishna, Effects of heat generation and absorption on thermal radiative MHD flow of chemically reacting Casson nanofluids over a wedge, *Case Stud. Therm. Eng.*, **65** (2025), 105637. https://doi.org/10.1016/j.csite.2024.105637
34. M. D. Kumar, J. L. D. Palencia, G. Dharmaiah, A. Wakif, S. Noeiaghdam, U. Fernandez-Gamiz, et al., ANFIS-PSO analysis on axisymmetric tetra hybrid nanofluid flow of Cu-CNT-Graphene-Tio_2 with WEG-Blood under linear thermal radiation and inclined magnetic field: A bio-medicine application, *Heliyon*, **11** (2025), e41429. https://doi.org/10.1016/j.heliyon.2024.e41429
35. M. J. Babu, Y. S. Rao, A. S. Kumar, C. S. K. Raju, S. A. Shehzad, T. Ambreen, et al., Squeezed flow of polyethylene glycol and water based hybrid nanofluid over a magnetized sensor surface: a statistical approach, *Int. Commun. Heat Mass*, **135** (2022), 106136. https://doi.org/10.1016/j.icheatmasstransfer.2022.106136
36. J. H. Mathews, K. D. Fink, *Numerical methods using MATLAB 4e*, New Jersey: New Jersey, 2004.
37. K. E. Atkinson, W. M. Han, D. Stewart, *Numerical solution of ordinary differential equations*, New York: John Wiley & Sons, 2009. https://doi.org/10.1002/9781118164495
38. B. L. Kuo, Application of the differential transformation method to the solutions of Falkner-Skan wedge flow, *Acta Mechanica*, **164** (2003), 161–174. https://doi.org/10.1007/s00707-003-0019-4
39. A. Ishak, R. Nazar, I. Pop, Falkner-Skan equation for flow past a moving wedge with suction or injection, *J. Appl. Math. Comput.*, **25** (2007), 67–83. https://doi.org/10.1007/BF02832339
40. S. M. Atif, S. Hussain, M. Sagheer, Heat and mass transfer analysis of time-dependent tangent hyperbolic nanofluid flow past a wedge, *Phys. Lett. A*, **383** (2019), 1187–1198. https://doi.org/10.1016/j.physleta.2019.01.003

AIMS Press